Polar Radiant Energy in the Far-Infrared Experiment (PREFIRE) Algorithm Theoretical Basis Document (ATBD) for the 2B-SFC data product

Xianglei Huang, Yan Xie, Xiuhong Chen,
Brian J. Drouin, Timothy I. Michaels, Erin Hokanson Wagner

R01 release, March/April 2025

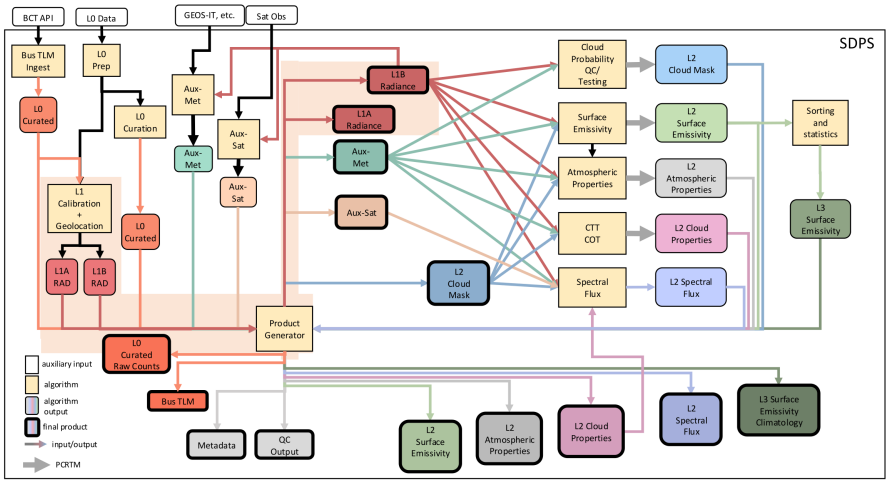

Figure 0.1: PREFIRE algorithm connectivity and flow.

Contents

1 Level-2 Spectral Emissivity

1.1 Introduction

This algorithm theoretical basis document (ATBD) describes the algorithm for the retrieval of surface spectral emissivity from top-of-atmosphere (TOA) spectral radiance. Specifically, this document describes the data, forward modeling, algorithm details and validation results of the retrieval studies based on an optimal estimation (OE) algorithm.

1.2 Data and forward modeling

1.2.1 ERA5 reanalysis data

ERA5 (ECMWF Reanalysis version 5) 6-hourly data (Hersbach et al. 2020) are used here to simulate clear-sky PREFIRE radiances at nadir view. Surface temperatures, atmospheric temperature and humidity profiles for four months (January, April, July and October 2005) in the Arctic from the ERA5 dataset will be used for the validation of the surface spectral emissivity retrieval algorithm.

1.2.2 Band-by-band surface emissivity dataset

A band-by-band surface emissivity dataset developed by Huang et al. (2016) is used in the study. This monthly-dependent global surface emissivity database is derived from first principles and observations, covering both mid-IR and far-IR at a $0.5^o \times 0.5^o$ spatial resolution.

1.2.3 PCRTM forward modeling

Forward simulations of TOA spectral radiance are performed using the Principal Component Radiative Transfer Model (PCRTM) (Liu et al. 2006) because it is both computationally affordable and accurate. In this study, the PCRTM is employed to generate the synthetic radiances and Jacobians on the PREFIRE spectra from 5 to 54 μm at 0.84 μm resolution. A more detailed description of the PCRTM can be found in the PREFIRE Spectral Flux (2B-FLX) ATBD. This model is used in the OE algorithm as the forward model.

1.3 OE Algorithm

Figure 1.1 illustrates the flow of the OE method surface emissivity algorithm.

1.3.1 PREFIRE channel selection

In this study, 14 PREFIRE channels in the mid-IR and far-IR are selected for the retrieval of surface spectral emissivity (Table 1.1). For monthly means of ERA5 6-hourly profiles in the Arctic Ocean, the transmittances in July are smaller than those in January, mostly due to the increase of water vapor abundance.

1.3.2 Optimal estimation retrieval

The optimal estimation method is a physical retrieval algorithm based on Bayes' theorem

$$(P(\mathbf{x} \mid \mathbf{y}) = \frac{(P(\mathbf{y} \mid \mathbf{x})P(\mathbf{x}))}{P(\mathbf{y})} \tag{1.1}$$

$P(\mathbf{x}|\mathbf{y})$ denotes the probability of a specific state $\mathbf{x}$ given the observation $\mathbf{y}$ and is known as the *a posteriori* probability density function (PDF). The state being optimized includes the geophysical variables

$$\{T_s, \epsilon_n\} \in \mathbf{x}, \mathbf{y} \tag{1.2}$$

The optimal estimation retrieval method seeks the $\mathbf{x}$ which maximizes this *a posteriori* PDF. $P(\mathbf{x}|\mathbf{y})$ can be calculated using the likelihood of observations given a specific state $P(\mathbf{y}|\mathbf{x})$ and the *a priori* probability distribution of the state $P(\mathbf{x})$. $P(\mathbf{y})$ functions as a normalization term and is not required in practice.

Observations ($\mathbf{y}$) at TOA contain both radiances and measurement noise. The PREFIRE observations are simulated by adding synthetic measurement noise ϵ to the clear-sky spectral radiances calculated by the PCRTM.

$$\mathbf{y} = \mathcal{F}(\mathbf{x}) + \epsilon \tag{1.3}$$

n	λ_n (μm)	Wavenumber edges ν_n (cm^{-1})	Transmittance in January	Transmittance in July
10	8.44	[1246.88, 1128.67]	0.85	0.73
12	10.13	[1030.93, 947.87]	0.80	0.73
13	10.97	[947.87, 877.96]	0.96	0.87
14	11.82	[877.96, 816.99]	0.96	0.83
15	12.66	[816.99, 764.53]	0.83	0.66
16	13.50	[764.53, 718.39]	0.48	0.35
20	16.88	[607.90, 578.03]	0.23	0.06
21	17.72	[578.03, 551.27]	0.45	0.10
22	18.57	[551.27, 526.59]	0.47	0.09
23	19.6	[526.59, 504.29]	0.39	0.05
24	20.25	[504.29, 483.79]	0.34	0.03
25	21.10	[483.79, 464.68]	0.28	0.02
26	21.94	[464.68, 447.23]	0.20	0.01
27	22.78	[447.23, 431.03]	0.16	0.00

Table 1.1: PREFIRE channels selected for the surface spectral emissivity retrieval. The atmospheric transmittances are calculated using MODTRAN5 with monthly and area mean profiles from ERA5 in January and July 2005 over the Arctic Ocean (73-77^{o}N, 0-360^{o}E).

The Gaussian distribution is widely used to model the PDFs due to its generality and convenience (Rodgers 2000). In this study, the likelihood $P(\mathbf{y}|\mathbf{x})$ and the *a priori* PDF $P(\mathbf{x})$ are assumed to be Gaussian. As a consequence, the *a posteriori* PDF $P(\mathbf{x}|\mathbf{y})$ also follows a Gaussian distribution.

$$\begin{gathered} \textit{A priori}\text{: } \mathbf{x} \approx \mathcal{N}(\mathbf{x_a}, \mathbf{S_a}) \\ \text{Likelihood: } \mathbf{y}|\mathbf{x} \approx \mathcal{N}(\mathcal{F}(\mathbf{x}), S_\epsilon) \\ \textit{A posteriori}\text{: } \mathbf{x}|\mathbf{y} \approx \mathcal{N}(\hat{\mathbf{x}}, \hat{\mathbf{S}}) \end{gathered}$$

$\mathbf{x_a}$ and $\mathbf{S_a}$ are the *a priori* mean and covariance matrix of the state $\mathbf{x}$, which represents the knowledge of state variables before observations. The observation $\mathbf{y}$ is composed of signals from the PCRTM forward model $\mathcal{F}$, given a specific state $\mathbf{x}$ and the noise quantified by the measurement error covariance matrix $\mathbf{S}_\epsilon$.

A priori knowledge of the state ($\mathbf{x}$) can be obtained from climatological data, laboratory measurements or empirical analysis. In this study, the *a priori* mean $\mathbf{x_a}$ values of surface spectral emissivity are set to 0.95 out of simplicity. The initial guess used in the iteration $\mathbf{x_0}$ is set equal to the *a priori* mean $\mathbf{x_a}$. The *a priori* covariance matrix $\mathbf{S_a}$ is derived from a recently developed surface emissivity database covering the far-IR spectrum (Huang et al. 2016). This global surface emissivity dataset is computed based on observations and first principles for each month at a $0.5^o \times 0.5^o$ spatial resolution. Monthly surface spectral emissivity at nadir view is first converted to the PREFIRE spectral grid.

For each PREFIRE channel, find the dataset spectral grids which fall within the channel range. Surface emissivity on the PREFIRE channel is computed as the mean of observationally-based surface emissivity at corresponding spectral grids.

A surface spectral emissivity dataset in the Arctic (60-90^{o}N, 0-360^{o}E) for all 12 calendar months is used to calculate the surface emissivity covariance matrix. The a priori covariance matrix S_a is generated by first multiplying the surface emissivity covariance matrix by 4, and then decreasing the correlation coefficient between different channels by half. This *a priori* constraint is neither too strict (so that signals from observations can be captured), nor too loose (so that surface emissivity estimates still fall within a reasonable range). The measurement error covariance $\mathbf{S}_\epsilon$ is a diagonal matrix of which the main diagonal is composed of the square of the PREFIRE noise equivalent spectral radiance.

$\hat{\mathbf{x}}$ is the optimal estimate of the state, of which the uncertainty can be characterized by the *a posteriori* covariance matrix $\hat{\mathbf{S}}$. Theoretical formulae of $\hat{\mathbf{x}}$ and $\hat{\mathbf{S}}$ can be conveniently derived based on Gaussian-distributed PDFs:

$$\hat{\mathbf{x}} = (\mathbf{K}^T {\mathbf{S}_\epsilon}^{-1} \mathbf{K} + {\mathbf{S}_\mathbf{a}}^{-1})^{-1} (\mathbf{K}^T {\mathbf{S}_\epsilon}^{-1} \mathbf{y} + {\mathbf{S}_\mathbf{a}}^{-1} \mathbf{x_a}) \tag{1.4}$$

$$\hat{\mathbf{S}} = (\mathbf{K}^T {\mathbf{S}_\epsilon}^{-1} \mathbf{K} + {\mathbf{S}_\mathbf{a}}^{-1})^{-1} \tag{1.5}$$

The optimal estimate $\hat{\mathbf{x}}$ can be viewed as a sum of the *a priori* mean and observed signal weighted by the inverse of the covariance matrices. The Jacobian matrix $\mathbf{K} = \delta F(\mathbf{x})/\delta \mathbf{x}$ describes the first derivative of the forward model with respect to a state variable.

For moderately linear cases, the Jacobian $\mathbf{K}$ can be used to invert observations in the measurement space back to the state space. Due to the dependence of Jacobian K on the state $\mathbf{x}$, it is necessary to iteratively solve the inverse problem and update the Jacobian at each iteration step. Therefore, the optimal estimation algorithm uses the iterative Gauss-Newton method to find the root of $\nabla_\mathbf{x} = -ln(P(\mathbf{x}|\mathbf{y})$. The retrieval process is governed by the following iteration steps:

$$\mathbf{x_{i+1}} = \mathbf{x_a} + (\gamma_a^{-1} + {\mathbf{K_i}}^T {\mathbf{S}_\epsilon}^{-1} \mathbf{K_i})^{-1} {\mathbf{K_i}}^T {\mathbf{S}_\epsilon}^{-1} [\mathbf{y} - \mathcal{F}(\mathbf{x_i}) + \mathbf{K_i}(\mathbf{x_i} - \mathbf{x_a})] \tag{1.6}$$

$$\mathbf{S_i} = (\gamma_a^{-1} + [\mathbf{K_i}]^T {\mathbf{S}_\epsilon}^{-1} \mathbf{K_i})^{-1} (\gamma^2 {\mathbf{S}_\mathbf{a}}^{-1} + {\mathbf{K_i}}^T {\mathbf{S}_\epsilon}^{-1} \mathbf{K_i}) (\gamma_a^{-1} + {\mathbf{K_i}}^T {\mathbf{S}_\epsilon}^{-1} \mathbf{K_i})^{-1} \tag{1.7}$$

Different from the classic formulations in Rodgers (2000), a tuning parameter γ is introduced to manually adjust the relative weight of *a priori* constraints and observed information (Carissimo et al. 2005, Zhou et al. 2007, Masiello et al. 2012, Turner et al. 2014). γ >1 means more information from the *a priori* than the observation. Following the work of Turner et al. (2014), a sequence of γ values [1000, 300, 100, 30, 10, 3, 1, 1, 1 ...] has been used in this study.

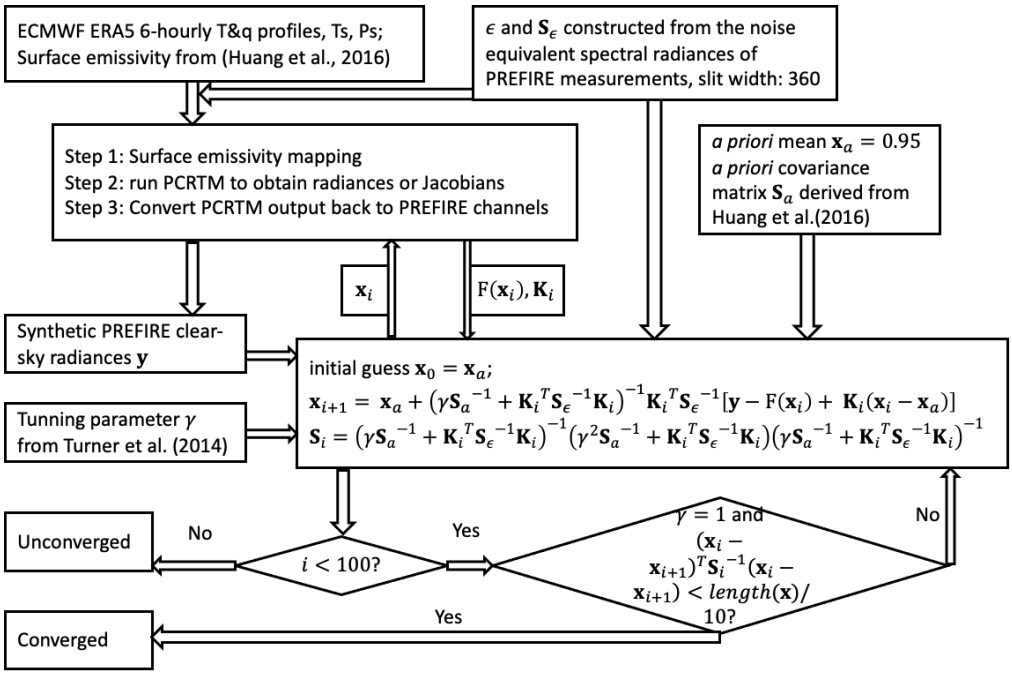

Figure 1.1: Flowchart of the optimal estimation algorithm for surface spectral emissivity retrieval on the PREFIRE channels.

This modification is meant to stabilize the retrieval process by gradually adding information from the observation step by step. The iteration will stop when γ=1 and the convergence criterion

$$((\mathbf{x_i} - \mathbf{x_{i+1}})^T [\mathbf{S_i}]^{-1} (\mathbf{x_i} - \mathbf{x_{i+1}}) < \frac{length(\mathbf{x})}{10} \tag{1.8}$$

is met. This convergence criterion ensures that the change of $\mathbf{x}$ between two steps is smaller than the retrieval uncertainty by at least an order of magnitude.

1.3.3 Surface emissivity mapping

The mapping process transforms surface spectral emissivity on the PREFIRE channels to the PCRTM (uses PCRTM sensor ID = 2) input spectrum composed of 740 grid cells from 50.38 to 2759.89 cm^{-1}. For each PCRTM spectral grid cell, if its wavenumber falls in any PREFIRE channel, the surface emissivity at this PCRTM spectral grid will be set equal to the value at that PREFIRE channel. If its wavenumber falls beyond the PREFIRE spectral range, the surface emissivity at this PCRTM spectral grid cell will be set equal to the value on the nearest PREFIRE channel — in other words, at $n = 10$ when wavenumber is less than 424.24 cm^{-1} or at $n = 27$ when wavenumber is greater than 1228.07 cm^{-1}. If its wavenumber does not fall in any selected PREFIRE channel but is still within

the PREFIRE spectral range, the surface emissivity at this PCRTM spectral grid will be set equal to the value at the nearest PREFIRE channel, or the average of two adjacent channels if the PCRTM wavenumber happens to fall in between two PREFIRE channels.

1.3.4 Conversion of PCRTM output back to the PREFIRE channels

The radiances and Jacobians generated by the PCRTM are for 5421 spectral grid cells from 50 to 2760 cm^{-1} at 0.5 cm^{-1} spectral resolution. This output spectrum differs from that of PREFIRE, which means the radiances and Jacobians need to be converted back to PREFIRE channels. To solve this problem, the spectral response function (SRF) and relevant spectrum information (v0.10.4_360_2021-03-28) are used. The SRF (size: 6951 $\times$ 63) is discretized in the spectral dimension into 6951 grid cells (0.43 - 60.00 μm at 0.0086 μm resolution) for each of the PREFIRE channels. The PCRTM output $\mathbf{Y_0}$ (size: 5421 $\times$ 1) is first interpolated onto the SRF spectral grid to get $\mathbf{Y_1}$ (size: 6951 $\times$ 1). For each selected PREFIRE channel, find the corresponding SRF column (size: 6951 $\times$ 1) and select SRF spectral grid cells which fall within the PREFIRE channel spectral range. If (1) the sum of SRF column is positive and (2) the sum of $\mathbf{Y_{1on}}$ of the selected spectral grid cell is an unmasked value, $\mathbf{Y_1}$ will then be convolved using the SRF column to derive $\mathbf{Y_2}$ on this PREFIRE channel.

$$\mathbf{Y_2} = \frac{\sum \mathbf{Y_1} \cdot SRFcolumn \cdot \Delta\lambda}{\sum SRFcolumn \cdot \Delta\lambda}, \Delta\lambda = 0.0086\mu m \tag{1.9}$$

Otherwise, the final output on this PREFIRE channel will be set as masked.

1.3.5 Information content analysis

The information content analysis aims to evaluate the information contributed by the true state, given noisy observations. In order to gain insight before the actual retrievals are conducted, monthly mean profiles in three typical polar regions [Arctic Ocean (73-77^{o}N, 0-360^{o}E), Greenland (70-80^{o}N, 310-340^{o}E), and Antarctic Plateau (75-85^{o}S, 60-90^{o}E)] from ERA5 6-hourly reanalysis data in January and July 2005 are used for the information content analysis.

Averaging kernel: The averaging kernel matrix, $\mathbf{A}$, (Backus et al. 1970) quantitatively evaluates the sensitivity of retrieval results to the true state.

$$\mathbf{A} = \frac{\delta \hat{\mathbf{x}}}{\delta \mathbf{x}} = \mathbf{S_a K}^T (\mathbf{K S_a K}^T + \mathbf{S}_\epsilon)^{-1} \mathbf{K} \tag{1.10}$$

The columns of $\mathbf{A}$ describe the response of retrieval estimates to the change of a specific true state variable. The rows of this averaging kernel matrix represent the sensitivity of a specific retrieval estimate to all state variables. The diagonal elements denote the sensitivity of a specific retrieval estimate to its own true value. This self-sensitivity is expected to be 1 in the ideal scenario.

Averaging kernels of surface emissivity in three typical polar regions (Arctic Ocean, Greenland, and Antarctic Plateau) are shown in Figure 1.2 for January

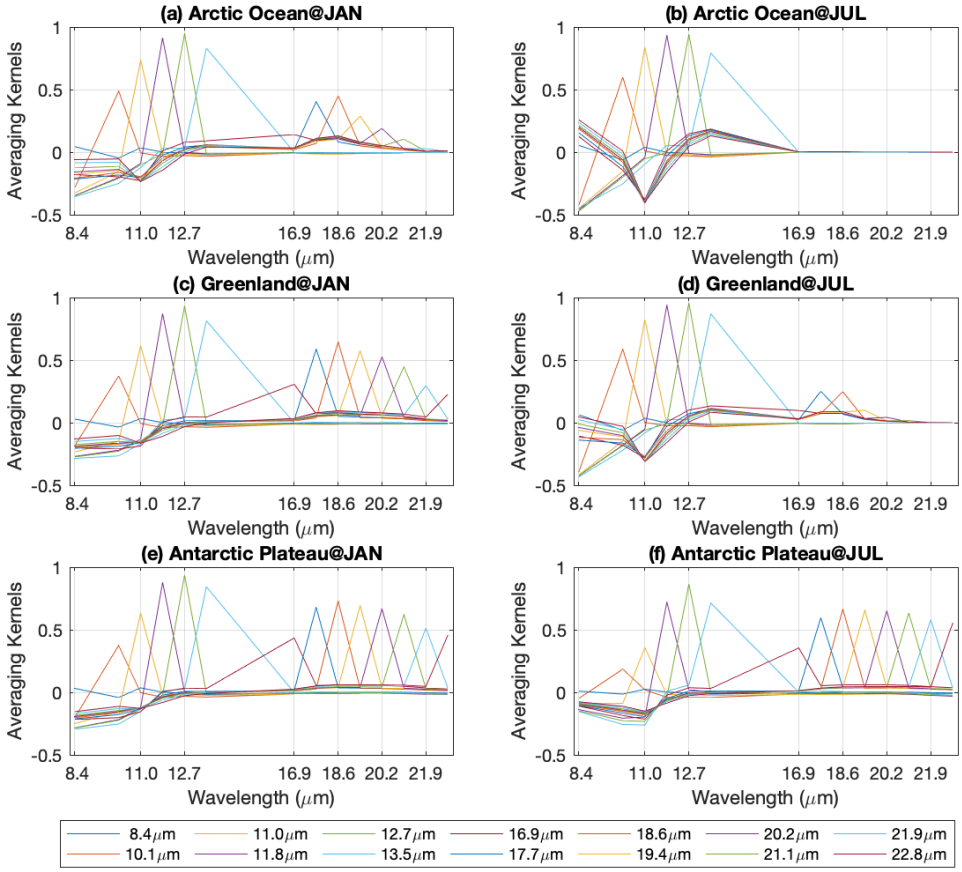

Figure 1.2: Averaging kernels of surface spectral emissivity in three typical polar regions: Arctic Ocean (73-77^{o}N, 0-360^{o}E), Greenland (70-80^{o}N, 310-340^{o}E), and Antarctic Plateau (75-85^{o}S, 60-90^{o}E). Calculated using ERA5 6-hourly reanalysis data for January and July 2005.

	Arctic Ocean		Greenland		Antarctic Plateau	
	JAN	JUL	JAN	JUL	JAN	JUL
d(T, q, T_s, ϵ_n)	9.6	8.4	10.9	8.6	11.8	11.8
$d(\epsilon_n)$	5.1	4.0	7.0	4.8	9.5	9.2
$d(\epsilon_{n_{MIR}})$	3.0	3.6	3.0	3.9	3.7	2.7
$d(\epsilon_{n_{FIR}})$	2.1	0.4	4.0	1.0	5.8	6.5
d(TCWV (cm))	0.30	1.27	0.12	0.59	0.07	0.02

Table 1.2: Degree of freedom, d, for signal and total column water vapor in three typical polar regions: Arctic Ocean (73-77^{o}N, 0-360^{o}E), Greenland (70-80^{o}N, 310-340^{o}E), and Antarctic Plateau (75-85^{o}S, 60-90^{o}E). Calculated using ERA5 6-hourly reanalysis data for January and July 2005.

and July in 2005. Each curve represents a row in the averaging kernel matrix. The *a priori* covariance matrix $\mathbf{S_a}$ is generated by first multiplying the emissivity covariance matrix by 4, and then decreasing the correlation coefficient between different channels by half. For the Arctic Ocean and Greenland, the peak values of MIR channels are larger than 0.5 in January and July. In contrast, the peak averaging kernel values of FIR channels decrease in July mostly due to increased water vapor absorption.

Degree of freedom for signal: The degree of freedom for signal d refers to the number of independent pieces of information concerning the true state that can be determined from a measurement. This value denotes how informative the observation can be, given the measurement noise and the dependence among state variables. Degree of freedom for signal equals the trace of the averaging kernel matrix, in other words, the sum of self-sensitivity.

$$d = tr(\mathbf{S_a K}^T(\mathbf{K S_a K}^T + \mathbf{S}_\epsilon)^{-1}\mathbf{K}) = tr(\mathbf{A}) \tag{1.11}$$

The d values for signals shown in Table 1.2 are based on the 58 valid PREFIRE longwave channels. The *a priori* covariance matrix $\mathbf{S_a}$ is generated by first multiplying the emissivity covariance matrix by 4, and then decreasing the correlation coefficient between different channels by half. The DOF for surface emissivity in the MIR varies around 3 to 4, despite the change of total column water vapor. Meanwhile, the d for signal surface emissivity in FIR decreases when the total column water vapor increases. This implies that surface emissivity retrieval in the FIR can be significantly influenced by the water vapor abundance.

1.3.6 OE Validation

Synthetic clear-sky PREFIRE radiances are used to validate the surface emissivity retrieval algorithm. There are 960 profiles including ERA5 6-hourly temperature and humidity, surface temperatures and pressures randomly chosen for January, April, July, October 2005 – 240 profiles for each month. Surface emissivity spectra from the surface spectral emissivity database (Huang et al.,

2016) are randomized by ±0.05, and adjusted to 0.98 if the emissivity values exceed 1. The atmospheric profiles and surface properties are then fed into the PCRTM V3.4 to generate the synthetic clear-sky PREFIRE radiances without noise. The synthetic measurement noises are randomly derived from the normal distribution with zero mean and one standard deviation characterized by the PREFIRE noise equivalent spectral radiances. This random noise is then added to the radiances to generate the synthetic clear-sky PREFIRE radiances with noise. Both synthetic radiances without and with noise are used to retrieve surface spectral emissivity. Differences between the retrieved surface emissivity and the true surface emissivity values, namely the input to PCRTM, are investigated. Retrieval results using synthetic radiances without noise can validate the performance of the optimal estimation retrieval algorithm. On the other hand, results using synthetic radiances with noise can examine the accuracy level of surface emissivity retrievals in practice given the PREFIRE instrument noise.

Figure 1.3 shows the mean and root mean square error (RMSE) of absolute differences between the surface emissivity retrievals and the true values, using clear-sky synthetic PREFIRE radiances without noise. All of the 960 cases in four months converged within 10 iterations. The optimal estimation retrieval algorithm performs steadily on the MIR channels, with the bias mean plus RMSE falling within the range [-0.02, 0.01]. For channels in the FIR, the mean of the absolute differences vary within ±0.01. Meanwhile, the corresponding RMSEs are between 0.02 and 0.03, larger than those in the MIR. This increase of RMSEs is mostly attributable to cases in July and October.

Figure 1.4 shows the mean and root mean square error (RMSE) of absolute differences between the surface emissivity retrievals and the true values, using clear-sky synthetic PREFIRE radiances with added instrument noise. Again, all of the 960 cases in four months converged within 10 iterations. The mean and RMSE of absolute differences show no significant difference compared to those in Figure **??**. With the currently expected PREFIRE instrument noise, the averaged surface emissivity retrieval will not be noticeably affected compared to the idealized retrieval without any noise.

1.3.7 An update to the OE algorithm

The algorithm can be applied to newer PREFIRE SRF data. We modified the PREFIRE SRF from version 10 (v0.10.4_360_2021-03-28) to version 12 (v12_2023-08-09). Version 12 has different SRFs for each of the two PREFIRE Thermal InfraRed Spectrometer (TIRS, or TIRS-PREFIRE) instruments. Each instrument has 8 sensors/scenes. For the same instrument, all 8 sensors/scenes have the same SRF, but have different Noise-Equivalent Delta Radiance (NEdR), see Figure **??**. We only do surface emissivity retrieval for channels with low NEdR. Table 1.3 lists the channels used for surface emissivity retrievals for each sensor/scene of TIRS1 and TIRS2. Then the results are expanded to all 58 PREFIRE longwave channels using interpolation.

As validation, the surface emissivity retrieval algorithm is applied to synthetic PREFIRE radiances. Then the retrieved surface emissivity is compared

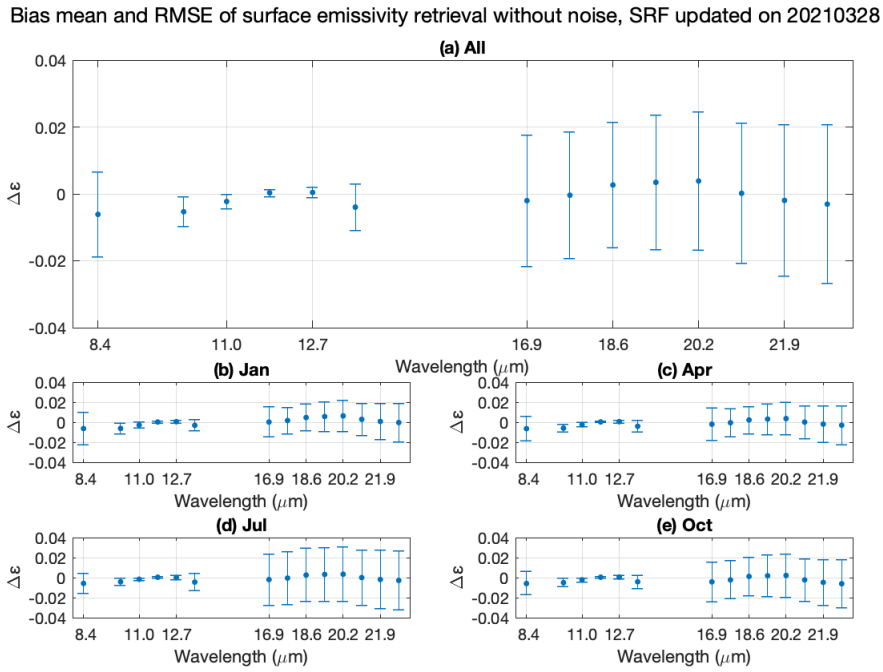

Figure 1.3: Mean (denoted by solid point markers) and Root Mean Square Error (denoted by bars) of absolute differences between the surface emissivity retrievals and the truth. The surface emissivity retrievals are derived from clear-sky synthetic PREFIRE radiances without noise. Panel (a) is based on retrieval results of all the converged cases. Subpanels (b), (c), (d), and (e) characterize retrieval results in January, April, July and October 2005 respectively.

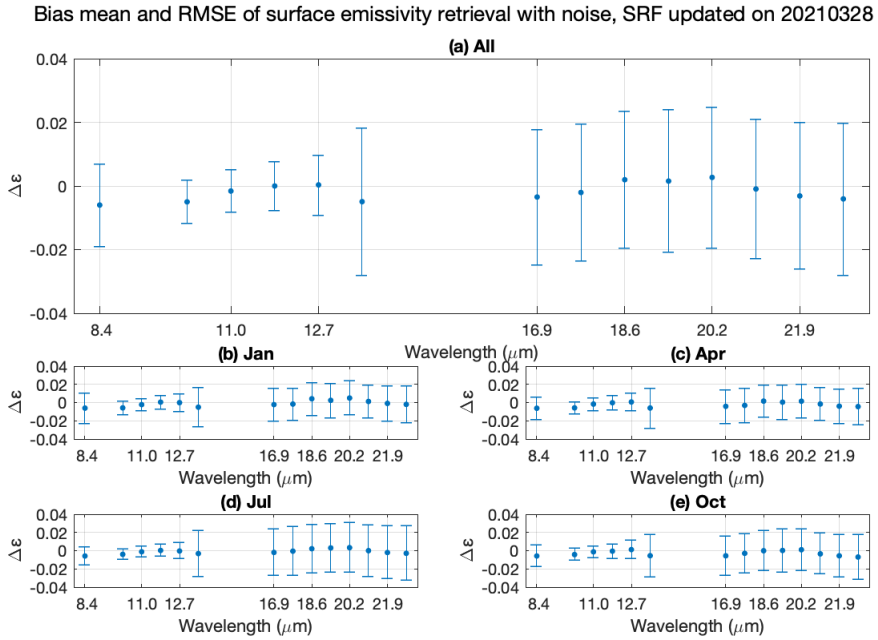

Figure 1.4: Similar to Figure 1.3 but for surface emissivity retrievals derived from clear-sky synthetic PREFIRE radiances with added instrument noise.

		Number of channels used	Channels used for retrieving surface emissivity
TIRS1	Sensor 1	14	10 12 13 14 15 16 20 21 22 23 24 25 26 27
	Sensor 2	13	10 13 14 15 16 20 21 22 23 24 25 26 27
	Sensor 3	9	10 14 15 16 23 24 25 26 27
	Sensor 4	14	10 12 13 14 15 16 20 21 22 23 24 25 26 27
	Sensor 5	14	10 12 13 14 15 16 20 21 22 23 24 25 26 27
	Sensor 6	14	10 12 13 14 15 16 20 21 22 23 24 25 26 27
	Sensor 7	10	10 12 13 14 15 16 20 22 26 27
	Sensor 8	12	10 12 13 14 15 16 20 21 23 24 25 26
TIRS2	Sensor 1	13	11 12 13 14 15 19 20 21 22 23 24 25 26
	Sensor 2	13	11 12 13 14 15 19 20 21 22 23 24 25 26
	Sensor 3	13	11 12 13 14 15 19 20 21 22 23 24 25 26
	Sensor 4	12	11 12 14 15 19 20 21 22 23 24 25 26
	Sensor 5	13	11 12 13 14 15 19 20 21 22 23 24 25 26
	Sensor 6	13	11 12 13 14 15 19 20 21 22 23 24 25 26
	Sensor 7	11	13 14 15 19 20 21 22 23 24 25 26
	Sensor 8	13	11 12 13 14 15 19 20 21 22 23 24 25 26

Table 1.3: Channels used for deriving surface emissivity for each sensor/scene of TIRS1 and TIRS2.

with true emissivity used for simulating synthetic PREFIRE radiances. The synthetic PREFIRE radiance is simulated from GEOS-FPIT (Goddard Earth Observing System Forward Processing for Instrument Teams) data for four months of 2021 (three days per month). Figures 1.5 and 1.6 show the mean and standard deviation of the difference between the retrieved and true emissivity. Generally, the mean difference and standard deviation are larger for detected clear-sky cases than for truly clear-sky cases. Table 1.4 summarizes the difference between retrieved and true surface emissivities for channels used in the retrieval. Overall, the median differences are all negative (about -0.01) and the RMSEs are about 0.015-0.020. There are very small differences between TIRS1 and TIRS2.

1.4 References

Backus, G., and F. Gilbert. (1970), "Uniqueness in the Inversion of Inaccurate Gross Earth Data." Philosophical Transactions of the Royal Society of London. Series A, Mathematical and Physical Sciences, vol. 266, no. 1173, pp. 123–192.

Carissimo, A., I. De Feis, and C. Serio. (2005), "The physical retrieval methodology for IASI: The δ-IASI code". Environ. Model. Software, 20, 1111-1126.

Ebell, K., Löhnert, U., Päschke, E., Orlandi, E., Schween, J. H., and Crewell, S. (2017), "A 1-D variational retrieval of temperature, humidity, and liquid cloud

Sensor / Scene	TIRS1 Sim Performance			TIRS1 Error Delta	TIRS2 Sim Performance			TIRS2 Error Delta
	5^{th}	95^{th}	median		5^{th}	95^{th}	median	
1	-0.027	0.015	-0.011	0.016	-0.030	0.016	-0.011	0.017
2	-0.023	0.014	-0.013	0.016	-0.025	0.016	-0.010	0.016
3	-0.035	0.011	-0.017	0.020	-0.019	0.018	-0.011	0.017
4	-0.019	0.016	-0.011	0.015	-0.024	0.014	-0.012	0.016
5	-0.037	0.016	-0.012	0.019	-0.028	0.015	-0.011	0.017
6	-0.022	0.016	-0.012	0.015	-0.024	0.015	-0.011	0.015
7	-0.021	0.018	-0.011	0.015	-0.026	0.010	-0.014	0.017
8	-0.024	0.015	-0.012	0.016	-0.024	0.014	-0.011	0.015
Aggregate	-0.025	0.016	-0.012	0.017	-0.025	0.015	-0.012	0.016

Table 1.4: 5^{th} and 95^{th} percentiles, median value, and error Delta (root mean square error) of the absolute difference between retrieved and true surface spectral emissivity for TIRS1 and TIRS2. The aggregate value is from the combination of all 8 sensors/scenes.

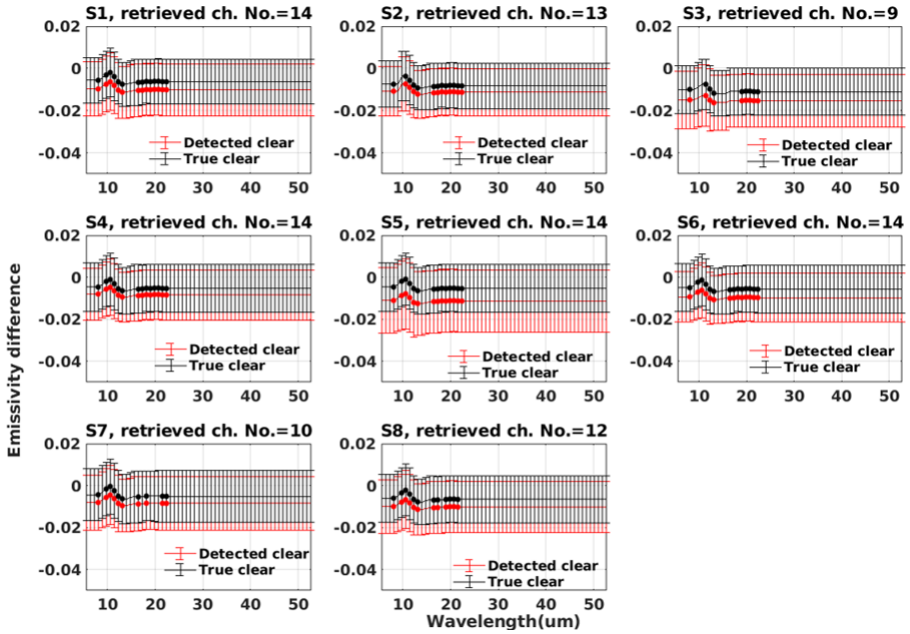

Figure 1.5: Mean and standard deviation of the difference between retrieved and true emissivity at PREFIRE channels for each sensor/scene of TIRS1 over the polar regions. The black line is for true clear-sky cases. The red line is for clear-sky cases as classified by the cloud mask algorithm. Dots are for the channels used for retrieval. Ticked vertical lines show the standard deviation of the difference.

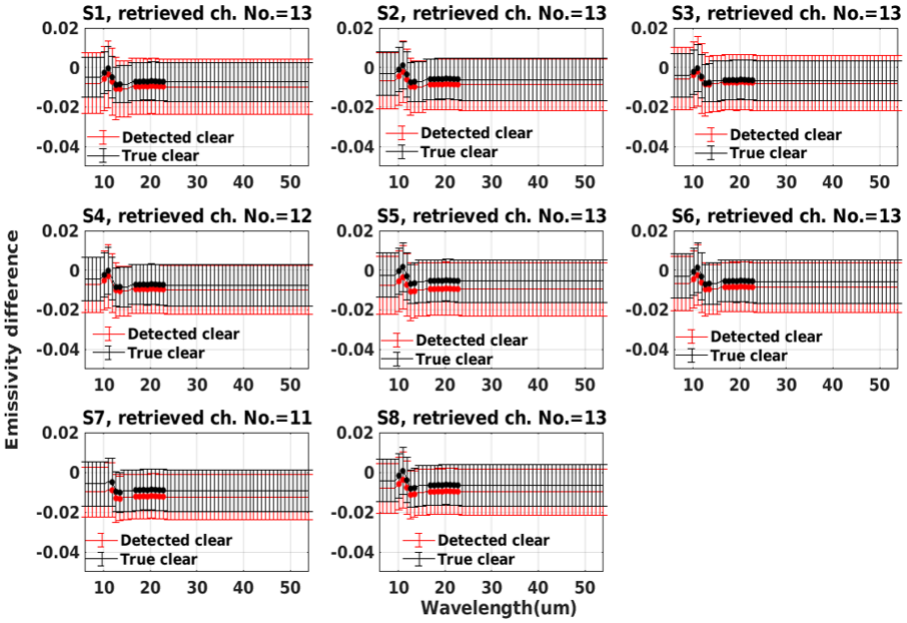

Figure 1.6: Same as Figure 1.5, but for TIRS2.

properties: Performance under idealized and real conditions". J. Geophys. Res. Atmos., 122, 1746– 1766, doi:10.1002/2016JD025945.

Hanel, R. A., Schlachman, B., Rogers, D., and Vanous, D. (1971), "Nimbus 4 Michelson Interferometer", Appl. Opt. 10, 1376-1382

Hersbach, H, Bell, B, Berrisford, P, et al. (2020), "The ERA5 global reanalysis". QJR Meteorol Soc., 146: 1999– 2049.

Huang, X., Chen, X., Zhou, D. K., & Liu, X. (2016), "An Observationally Based Global Band-by-Band Surface Emissivity Dataset for Climate and Weather Simulations", Journal of the Atmospheric Sciences, 73(9), 3541-3555.

Liu, X., Smith, W. L., Zhou, D. K, and Larar, A. (2006), "Principal component-based radiative transfer model for hyperspectral sensors: theoretical concept", Appl. Opt. 45, 201-209

Masiello, G., Serio, C. and Antonelli, P. (2012), "Inversion for atmospheric thermodynamical parameters of IASI data in the principal components space", Q.J.R. Meteorol. Soc., 138: 103-117.

Milstein, A. B. and Blackwell W. J.(2016), "Neural network temperature and

moisture retrieval algorithm validation for AIRS/AMSU and CrIS/ATMS," Journal of Geophysical Research: Atmospheres. 10.1002/2015JD024008

Rodgers, C. D. (2000). "Inverse Methods for Atmospheric Sounding: Theory and Practice", World Scientific.

Turner, D. D., & L ohnert, U. (2014). "Information Content and Uncertainties in Thermodynamic Profiles and Liquid Cloud Properties Retrieved from the Ground-Based Atmospheric Emitted Radiance Interferometer (AERI)", Journal of Applied Meteorology and Climatology, 53(3), 752-771.

Xie, Y., Huang X., Chen X., L'Ecuyer T.S., Drouin B.J., and Wang J. (2022), "Retrieval of Surface Spectral Emissivity in Polar Regions Based on the Optimal Estimation Method," Journal of Geophysical Research (Atmospheres), 127, e2021JD035677. https://doi. org/10.1029/2021JD035677.

Yang, Z., Chen X., Huang X., L'Ecuyer T. and Drouin B. (2023), "A Fast Neural Network-Based Approach for Joint MID-IR and FAR-IR Surface Spectral Emissivity Retrieval," IGARSS 2023 - 2023 IEEE International Geoscience and Remote Sensing Symposium, Pasadena, CA, USA, 2023, pp. 5324-5327, doi: 10.1109/IGARSS52108.2023.10281903.

Zhou, D. K., Smith, W. L., Sr., Liu, X., Larar, A. M., Mango, S. A., & Huang, H. (2007). "Physically Retrieving Cloud and Thermodynamic Parameters from Ultraspectral IR Measurements", Journal of the Atmospheric Sciences, 64(3), 969-982.

2 Appendix

2.1 Table of variables and symbols

$\mathbf{A}$	averaging kernel matrix
α	angular resolution
β	azimuth angle
B	blackbody radiance
BW	spectral bandwidth
χ	convergence criterion
c	speed of light, cost function
CED	Cloud particle Effective Diameter
COD	Cloud Optical Depth
CTP	Cloud Top Pressure
CWP	Cloud Water Path
d	degree of freedom
ε	emissivity
ϵ	noise, error
ϕ	longitude
E	irradiance
F	flux
f	focal length
$\mathcal{F}$	function
γ	*a priori* weight
G	gravitational constant
g	gain
H	height
h	Planck's constant
I	radiance
IC	Information Content
IWC	Ice Water Content
IWP	Ice Water Path
j	counter
k	Boltzmann's constant, unknown
$\mathbf{K}$	Jacobian
λ	wavelength, Marquardt-Levenberg parameter
l	distance
L	radiance
LTS	Lower Tropospheric Stability
LWC	Liquid Water Content
LWP	Liquid Water Path
M	counter, mass
m	number of along-track frames
$\mathcal{M}$	matrix

N	counter
n	channel
$\mathcal{N}$	normal distribution
ν	frequency
NEdT	Noise-Equivalent delta Temperature
o	offset
Ω	solid angle
p	pressure
P	probability
PWV	Precipitable Water Vapor
Q	water vapor
ρ	reflection coefficient
R	radius, resistance, cost-function change
$\Re$	response function
$\wp$	responsivity
σ_B	Stefan-Boltzmann constant
$\mathbb{S}$	signal level in digitized counts
S	covariance
SI	Segmentation Index
SNR	Signal-to-Noise Ratio
SRF	Spectral Response Function
θ	latitude, potential temperature, polar coordinate angle
τ	transmission, optical depth
T	temperature
TR	Training Radiances
TREM	TRaining Eigenvector Matrices
t	time
ϕ	polar coordinate angle
V	voltage
v	velocity
x, y, z	position coordinates
z	convergence, standard deviation of scaled differences
$\mathbf{x}$	state vector
X	focal plane position
$\mathbf{y}$	measurement vector
Y	focal plane position
ζ	incidence angle

Table 2.1: Table of variables and symbols.

2.2 Abbreviations and acronyms

ADM	Angular Distribution Model
AIRS	Atmospheric Infrared Sounder
ATBD	Algorithm Theoretical Basis Document
CERES	Clouds and the Earth's Radiant Energy System
DEM	Digital Elevation Model
DOF	Degree of Freedom
ECI	Earth-Centered Inertial
ECMWF	European Centre for Medium-Range Weather Forecasts
EOF	Empirical Orthogonal Function
FIR	Far-InfraRed
FOV	Field Of View
FPA	Focal Plane Array
FWHM	Full Width at Half Maximum
GEOS-IT	Goddard Earth Observing System for Instrument Teams
GMAO	Global Modelling and Assimilation Office
IFOV	Instantaneous Field Of View
IFS	Integrated Forecasting System
LW	Longwave
MIR	Mid-InfraRed
NASA	National Aeronautics and Space Administration
NEP	Noise Equivalent Power
NEdR	Noise Equivalent delta spectral Radiance
OE	Optimal Estimation
OLR	Outgoing Longwave Radiation
PCRTM	Principal Component-based Radiative Transfer Model
PREFIRE	Polar Radiant Energy in the Far-InfraRed Experiment
ROIC	Read-Out Integrated Circuit
RMSE	Root Mean Square Error
SDPS	Science Data Processing System
SSF	Single Scanner Footprint
SRF	Spectral Response Function
TCWV	Total Column Water Vapor
TIRS	(TIRS-PREFIRE) Thermal InfraRed Spectrometer
TIRS1	Thermal InfraRed Spectrometer on PREFIRE-SAT1
TIRS2	Thermal InfraRed Spectrometer on PREFIRE-SAT2
TOA	Top of Atmosphere
UTC	Coordinated Universal Time
VZA	Viewing Zenith Angle
WV	Wavelength

Table 2.2: Abbreviations and acronyms.

2.3 Figure listing with links

Table 2.3: List of Figures in this ATBD.

Table of Contents	
0.1	PREFIRE algorithm connectivity and flow
Emissivity Algorithm	
1.1	OE algorithm flowchart
1.2	OE averaging kernels
1.3	OE error estimates, noise-free
1.4	OE error estimates with instrument noise
1.5	OE truth difference for TIRS1
1.6	OE truth difference for TIRS2